GLOBAL BIOGEOCHEMICAL CYCLES, VOL. 23, GB1003, doi:10.1029/2008GB003316, 2009

# Natural variability and anthropogenic trends in oceanic oxygen in a coupled carbon cycle–climate model ensemble

T. L. Frölicher,[1] F. Joos,[1,2] G.-K. Plattner,[3] M. Steinacher,[1] and S. C. Doney[4]

Received 22 July 2008; revised 20 October 2008; accepted 3 December 2008; published 13 February 2009.

[1] Internal and externally forced variability in oceanic oxygen ($O_2$) are investigated on different spatiotemporal scales using a six-member ensemble from the National Center for Atmospheric Research CSM1.4-carbon coupled climate model. The oceanic $O_2$ inventory is projected to decrease significantly in global warming simulations of the 20th and 21st centuries. The anthropogenically forced $O_2$ decrease is partly compensated by volcanic eruptions, which cause considerable interannual to decadal variability. Volcanic perturbations in oceanic oxygen concentrations gradually penetrate the ocean's top 500 m and persist for several years. While well identified on global scales, the detection and attribution of local $O_2$ changes to volcanic forcing is difficult because of unforced variability. Internal climate modes can substantially contribute to surface and subsurface $O_2$ variability. Variability in the North Atlantic and North Pacific are associated with changes in the North Atlantic Oscillation and Pacific Decadal Oscillation indexes. Simulated decadal variability compares well with observed $O_2$ changes in the North Atlantic, suggesting that the model captures key mechanisms of late 20th century $O_2$ variability, but the model appears to underestimate variability in the North Pacific. Our results suggest that large interannual to decadal variations and limited data availability make the detection of human-induced $O_2$ changes currently challenging.

**Citation:** Frölicher, T. L., F. Joos, G.-K. Plattner, M. Steinacher, and S. C. Doney (2009), Natural variability and anthropogenic trends in oceanic oxygen in a coupled carbon cycle–climate model ensemble, *Global Biogeochem. Cycles*, *23*, GB1003, doi:10.1029/2008GB003316.

## 1. Introduction

[2] Understanding mechanisms of ocean variability on time scales from months to centuries is key to interpreting observed oceanic changes in the context of natural and anthropogenic climate change. While climatological mean states of circulation patterns, tracer distributions and biogeochemical cycles are well studied [e.g., *Garcia et al.*, 2006; *Key et al.*, 2004], much less attention has been given to the variability in the coupled climate-biogeochemical system. Ensemble simulations are necessary in order to extract the climate signal in response to a certain external forcing from the natural internal variability of the climate system. The use of an ensemble of model simulations, each forced by identical boundary conditions but started at different initial conditions, is standard to investigate variability and trends in the physical climate system [*Meehl et al.*, 2007]. However, ensemble simulations have so far hardly been used for coupled climate-biogeochemical analyses.

[3] The concentration of dissolved oxygen in the thermocline and the deep ocean is a particularly sensitive indicator of change in ocean transport and biology [*Joos et al.*, 2003]. Less than a percent of the combined atmosphere and ocean $O_2$ inventory is found in the ocean. The $O_2$ concentration in the ocean interior reflects the balance between $O_2$ supply from the surface through physical transport and $O_2$ consumption by respiration of organic material.

[4] Oxygen concentrations in the ocean are expected to change under anthropogenic climate change. Surface warming, an increase in stratification, a reduction in the meridional overturning circulation, and reduced ventilation of the thermocline, as partly expected under anthropogenic global warming [*Meehl et al.*, 2007], will tend to reduce the transport of oxygen-rich surface waters to the deep and to decrease the ocean's oxygen inventory. Reduced upwelling of nutrient-rich waters tends to reduce export production of organic material and respiratory oxygen consumption in subsurface water, but tends to increase the residence time of water in the deep ocean, allowing for more oxygen consumption.

---

[1] Climate and Environmental Physics, University of Bern, Bern, Switzerland.

[2] Oeschger Centre for Climate Change Research, University of Bern, Bern, Switzerland.

[3] Environmental Physics, Institute of Biogeochemistry and Pollutant Dynamics, ETH Zurich, Zurich, Switzerland.

[4] Marine Chemistry and Geochemistry, Woods Hole Oceanographic Institution, Woods Hole, Massachusetts, USA.

0886-6236/09/2008GB003316$12.00

[5] Recent observations of oceanic oxygen changes show decreasing trends over the last decades in the circumpolar region, in middle and high latitudes of the North Pacific, in the eastern South Pacific and in the North Atlantic [*Emerson et al.*, 2004]. *Stramma et al.* [2008] reported a decline in $O_2$ in tropical oceans and an expanding of Oxygen Minimum Zones during the past 50 years. However, there are also regions where oxygen has recently increased such as the southern Indian Ocean [*McDonagh et al.*, 2005] and the boundary region between the subpolar and subtropical gyres in the North Pacific [*Mecking et al.*, 2008], possibly reflecting natural variability. The observed changes over the last several decades in dissolved oxygen range from about $-80$ to $+10$ $\mu$mol kg$^{-1}$, and can amount to up to 50% of the total dissolved oxygen in oxygen-poor regions. Whether observed changes in dissolved oxygen are the result of natural variability or of anthropogenic influences is still an open question. The presence of large-scale propagating $O_2$ anomalies [*Deutsch et al.*, 2006], the short lengths of the observational records, and the relatively small number of regions with repeat sampling complicate the detection of long-term trends associated with anthropogenic climate change and make it difficult to extrapolate available observations of trends in dissolved $O_2$ to individual basins [*Keller et al.*, 2002] or even to the globe.

[6] Earlier modeling studies rely on results from single atmosphere-ocean general circulation model (AOGCM) simulations [*Matear and Hirst*, 2003; *Bopp et al.*, 2002], from coupled climate-biogeochemical models of reduced complexity [*Schmittner et al.*, 2008; *Plattner et al.*, 2002, 2001], or from ocean only simulations of the North Pacific [*Deutsch et al.*, 2006]. These authors all found that dissolved oxygen is a sensitive indicator of climate change. The coupled model results suggest that anthropogenic forcing causes a net loss of oxygen to the atmosphere, mainly driven by changes in circulation and to a lesser extent by surface warming. Several studies have investigated the volcanic imprint on physical atmospheric and oceanic properties [e.g., *Church et al.*, 2005], but there has been little focus on volcanic impacts on biogeochemical tracers [*Jones and Cox*, 2001]. *Plattner et al.* [2002] found with their zonally averaged, 2-D ocean model that cooling from volcanic forcing affects the net air-sea flux of oxygen considerably by reversing the anthropogenically driven outgassing for a few years.

[7] Here, we analyze for the first time $O_2$ variability in an ensemble of simulations and from a set of sensitivity simulations with the Climate System Model of the National Center for Atmospheric Research, NCAR CSM1.4-carbon [*Fung et al.*, 2005; *Doney et al.*, 2006; *Steinacher et al.*, 2008] over the industrial period and the 21st century. The goals are to (1) characterize variability in dissolved oxygen from annual to decadal to century time scales, (2) quantify the role of internal unforced variability, natural forced variability by explosive volcanism and anthropogenic change, (3) relate modeled changes in oxygen to different physical and biological mechanisms and to climate modes such as the North Atlantic Oscillation (NAO) and the Pacific Decadal Oscillation (PDO), and (4) compare model statistics of change with available observations of decadal-scale changes in dissolved oxygen. A particular emphasis is on externally forced variability from volcanic eruptions, a natural forcing for which the impact on oceanic $O_2$ variability has not yet been investigated in detail.

## 2. Methods

### 2.1. Model

[8] Simulations were performed with the NCAR CSM1.4-carbon coupled climate-carbon cycle model [*Doney et al.*, 2006; *Fung et al.*, 2005]. The core of the model is a modified version of the NCAR CSM1.4 coupled physical model, consisting of ocean, atmosphere, land and sea ice components integrated via a flux coupler without flux adjustments [*Boville et al.*, 2001; *Boville and Gent*, 1998]. The atmospheric model CCM3 is run with a spectral truncation resolution of $\sim$3.75° (T31 grid) and 18 levels in the vertical [*Kiehl et al.*, 1998]. The NCAR CSM Ocean Model (NCOM) is noneddy resolving with 25 vertical levels and a resolution of 3.6° in longitude and 0.8° to 1.8° in latitude (T31 × 3 grid) [*Gent et al.*, 1998]. The dynamical sea ice model is run at the resolution of the ocean model, and the land surface model is run at the resolution of the atmospheric model. CSM1.4-carbon includes a modified version of the terrestrial biogeochemistry model Carnegie-Ames-Stanford Approach (CASA) [*Randerson et al.*, 1997], and a derivate of the Ocean Carbon-Cycle Model Intercomparison Project Phase 2 (OCMIP-2) oceanic biogeochemistry model [*Najjar et al.*, 2007]. Ocean ecosystem dynamics are not explicitly calculated in the model. The CSM1.4-carbon source code discussed here is described in detail by *Doney et al.* [2006] and section 1 of the auxiliary material.[1]

[9] Overall, the NCAR CSM1.4-carbon climatological mean state of $O_2$ and $O_2$ flux results are broadly consistent with global ocean observations and similar to other coarse resolution carbon cycle simulations [*Najjar et al.*, 2007; *Doney et al.*, 2006]. The model is able to adequately represent large-scale oxygen patterns (see section 2 in the auxiliary material). Shortcomings of the model are the overestimation of $O_2$ in the North Pacific due to deficiencies in the model circulation and export of organic matter as well as an underestimation of $O_2$ in the equatorial Atlantic thermocline due to excess upwelling and nutrient trapping. More information on strengths and weaknesses of the NCAR model can be found in the works by *Doney et al.* [2006] and *Najjar et al.* [2007], where modeled physical and biogeochemical fields are discussed and compared to observations and/or other ocean carbon cycle models.

### 2.2. Experimental Design

[10] A total of 11 simulations have been performed with the CSM1.4-carbon over the period 1820 to 2100 AD: (1–6) An ensemble of six transient simulations over the historical period followed by the IPCC SRES A2 emission scenario after year 2000 and (7) a single historical simulation followed by the IPCC B1 scenario, (8–10) a three-member ensemble from 1955 to 2000 AD branching off from three of the six transient simulations but where historical

---

[1] Auxiliary materials are available in the HTML. doi:10.1029/2008GB003316.

volcanic eruptions were omitted, and (11) a 480-year control simulation. Each of the six ensemble integrations branches off at different El-Niño Southern Oscillation state drawn from an approximately stable 1000-year preindustrial carbon–climate control experiment [*Doney et al.*, 2006].

[11] For the period 1820 to 2000, $CO_2$ emissions were prescribed using historical emissions from fossil fuel burning [*Andres et al.*, 1999; *Marland and Rotty*, 1984] and land use change (Figure 1a). The land use change is simply treated as an external source of $CO_2$ to the atmosphere and doesn't alter the prognostic land carbon pools in the model. The land use emission history of *Houghton* [1999] has been scaled with a single scaling factor of 0.7 to match observed atmospheric $CO_2$ in year 2000. The scaling factor has been estimated by combining results from a fossil emission only simulation with the CSM1.4-carbon model and a range of simulations with the cost-efficient Bern model [*Joos et al.*, 1996].

[12] Observation-based time histories of solar irradiance [*Wang et al.*, 2005], spatially explicit aerosol loading from explosive volcanism [*Ammann et al.*, 2003], non-$CO_2$ greenhouse gases $CH_4$, $N_2O$, CFC-11 and CFC-12, other halogenated species and $SF_6$, and anthropogenic sulfate aerosols with a recurring annual cycle of ozone and natural sulfate aerosol have also been included [*Joos et al.*, 2001; *Ammann et al.*, 2007]. Volcanic aerosols were specified as a single aerosol size distribution by converting ice core aerosol proxies to meridionally and temporally varying atmospheric aerosol fields following *Ammann et al.* [2003]. The volcanic forcing was diagnosed using a conversion factor between radiative forcing and prescribed visible optical depth [*Ammann et al.*, 2007]. Atmospheric $CH_4$, $N_2O$, CFC-11 and CFC-12 were individually prescribed following ice core measurements and direct atmospheric observations. The CFC-11 concentration is adjusted for the greenhouse warming effect of other halogenated species concentrations besides CFC-11 and CFC-12.

[13] For the period 2000 to 2100, carbon and anthropogenic sulfur emissions were prescribed following the illustrative SRES emissions scenario A2 (Figure 1a) [*Intergovernmental Panel on Climate Change*, 2000]. A single simulation from 2000 to 2100 AD following the SRES scenario B1 complements the ensemble. Non-$CO_2$ greenhouse gas concentrations are prescribed following *Forster et al.* [2007]. The solar irradiance is set to 1366.12 W $m^{-2}$, averaged from 1978 to 1999, and no volcanic eruptions are assumed.

[14] In order to isolate the volcanic signal from other external forced variability, we additionally run a three-member ensemble, branching off from three of the six transient simulations from 1955 to 2000, where volcanic forcing is omitted. A 480-year control simulation in which $CO_2$ emissions are set to zero and other forcings are set to be constant at preindustrial levels is used to detrend model results (see section 3 in the auxiliary material for details).

### 2.3. Analysis Methods

[15] The statistical significance of externally forced $O_2$ changes and of the correlation coefficients between $O_2$ and different climate modes are calculated using two-sided Student's *t* test (p value $< 0.05$). Temporal changes in the $O_2$ and AOU distribution in the ocean can be broken down into individual components that can be identified with different drivers (equations (1)–(4)):

$$\Delta O_2 = \Delta O_2^{\mathrm{sat}} + \Delta O_2^{\mathrm{soft}} + \Delta O_2^{\mathrm{dis}}, \tag{1}$$

$$\Delta O_2^{\mathrm{sat}} = \Delta O_2 + \Delta \mathrm{AOU}, \tag{2}$$

$$\Delta O_2^{\mathrm{soft}} = r_{O_2:PO_4} \Delta PO_4, \tag{3}$$

$$\Delta O_2^{\mathrm{dis}} = \Delta \mathrm{AOU}^{\mathrm{gasex}} = -\Delta \mathrm{AOU} - r_{O_2:PO_4} \Delta PO_4. \tag{4}$$

The concept is analogous to that used for dissolved inorganic carbon described by *Sarmiento and Gruber* [2006]. First, the sum of $O_2$ and AOU (AOU = $O_2^{sat}$ − $O_2$), $O_2^{sat}$, is by definition the saturated concentration of oxygen, which is a function of temperature and salinity. This corresponds to the so-called potential solubility pump for dissolved inorganic carbon [*Volk and Hoffert*, 1985]. Second, AOU is further split into a contribution from the cycling of organic matter, $O_2^{soft}$, sometimes referred to as soft-tissue pump [*Sarmiento and Gruber*, 2006], and a component related to the gas exchange of AOU ($O_2^{dis}$). $O_2^{soft}$ includes changes in $O_2$, via Phosphate ($PO_4$), due to changes in production/remineralization and changes in $O_2$ (resp. $PO_4$) driven by circulation/ventilation changes. The stoichiometric $O_2$ to $PO_4$ ratio for production and remineralization, $r_{O_2:PO_4}$, is fixed in the model at −170 according to *Anderson and Sarmiento* [1994]. Note that $O_2^{soft}$ does not contribute to the overall increase/decrease in global ocean oceanic oxygen. It only accounts for ocean interior redistributions because total $PO_4$ remains constant in the model. Changes in $O_2^{dis}$ include all the contributions to air-sea gas exchange resulting from surface ocean changes associated with $O_2^{sat}$ and $O_2^{soft}$. Unfortunately, a separation into the two components is not straightforward. Hence, uptake and release of $O_2$ by/from the ocean as a consequence of ocean interior redistributions will be attributed to $O_2^{dis}$. Changes in ventilation and circulation have an impact on both $O_2^{soft}$ and $O_2^{dis}$. Note that we use an approach to separate individual mechanisms contributing to the overall changes in modeled oceanic $O_2$ in our coupled AOGCM that is different from the approaches used in previous studies by *Deutsch et al.* [2006], *Plattner et al.* [2002], and *Bopp et al.* [2002], involving running a series of additional sensitivity studies, an approach not feasible with the coupled AOGCM ensemble because of the lack of computational resources.

## 3. Results

### 3.1. Global Mean Changes

[16] We start the analysis by first describing the global mean evolution of key variables to characterize the simulations (Figures 1b–1f). Unless otherwise stated, changes

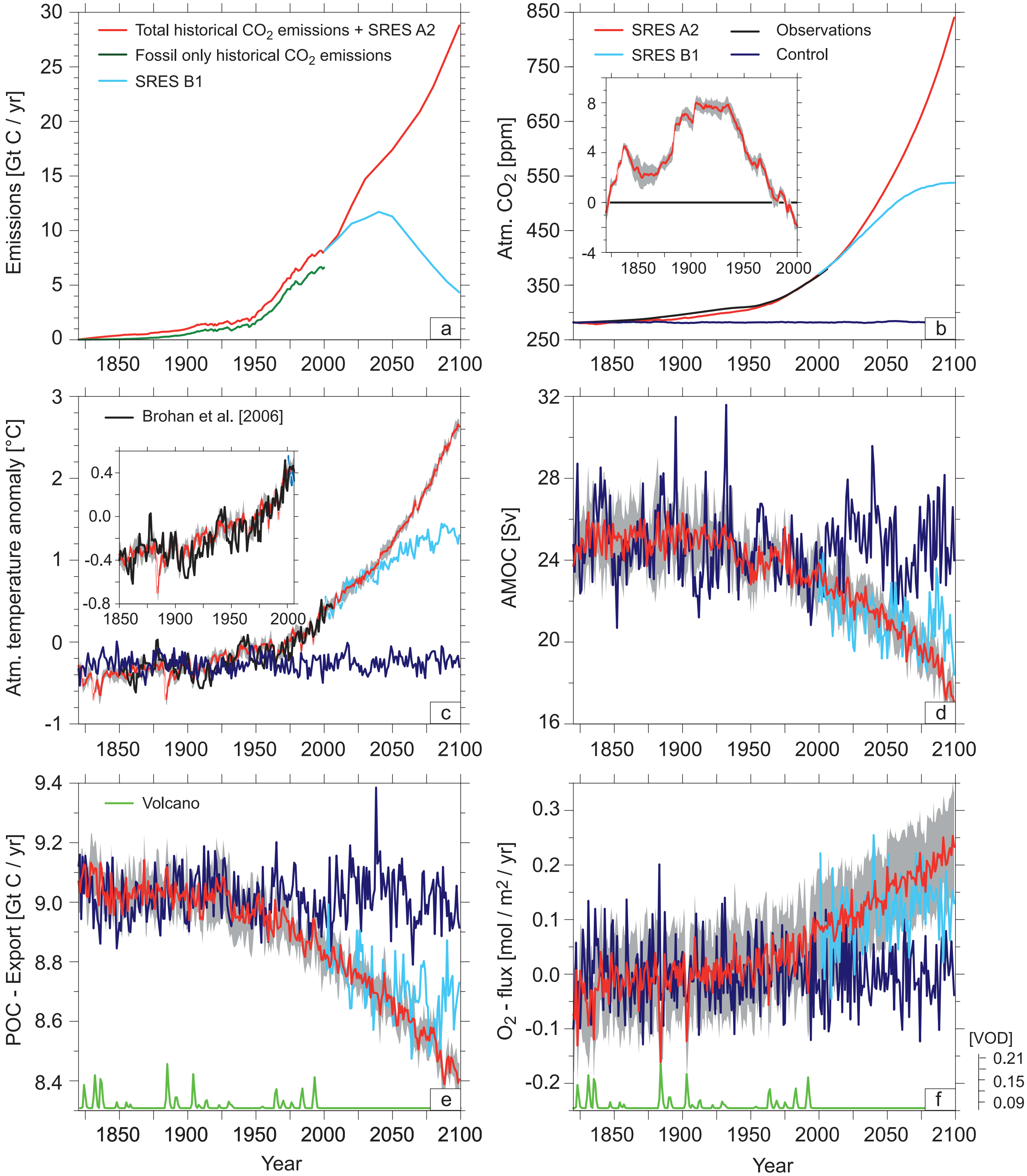

**Figure 1.** Overview of simulated global ensemble mean results from 1820 to 2100 AD. (a) Prescribed carbon emissions. Scaled land use emissions are visible as the difference between total emissions (red) and fossil only emissions (green); (b) simulated atmospheric annual mean $CO_2$ and deviations between observed and simulated atmospheric $CO_2$ from 1820 to 2006 AD; (c) change in annual mean atmospheric surface temperature; (d) maximum strength of the annual mean North Atlantic overturning stream function; (e) export of particulate organic carbon (POC export) out of the production zone (75 m); (f) offset-corrected sea-to-air $O_2$ flux. Volcanic forcing is expressed as visible optical depth (right *y* axis in Figure 1f) and is indicated by the green line. The gray shaded bands indicate 1-$\sigma$ confidence interval of the ensemble.

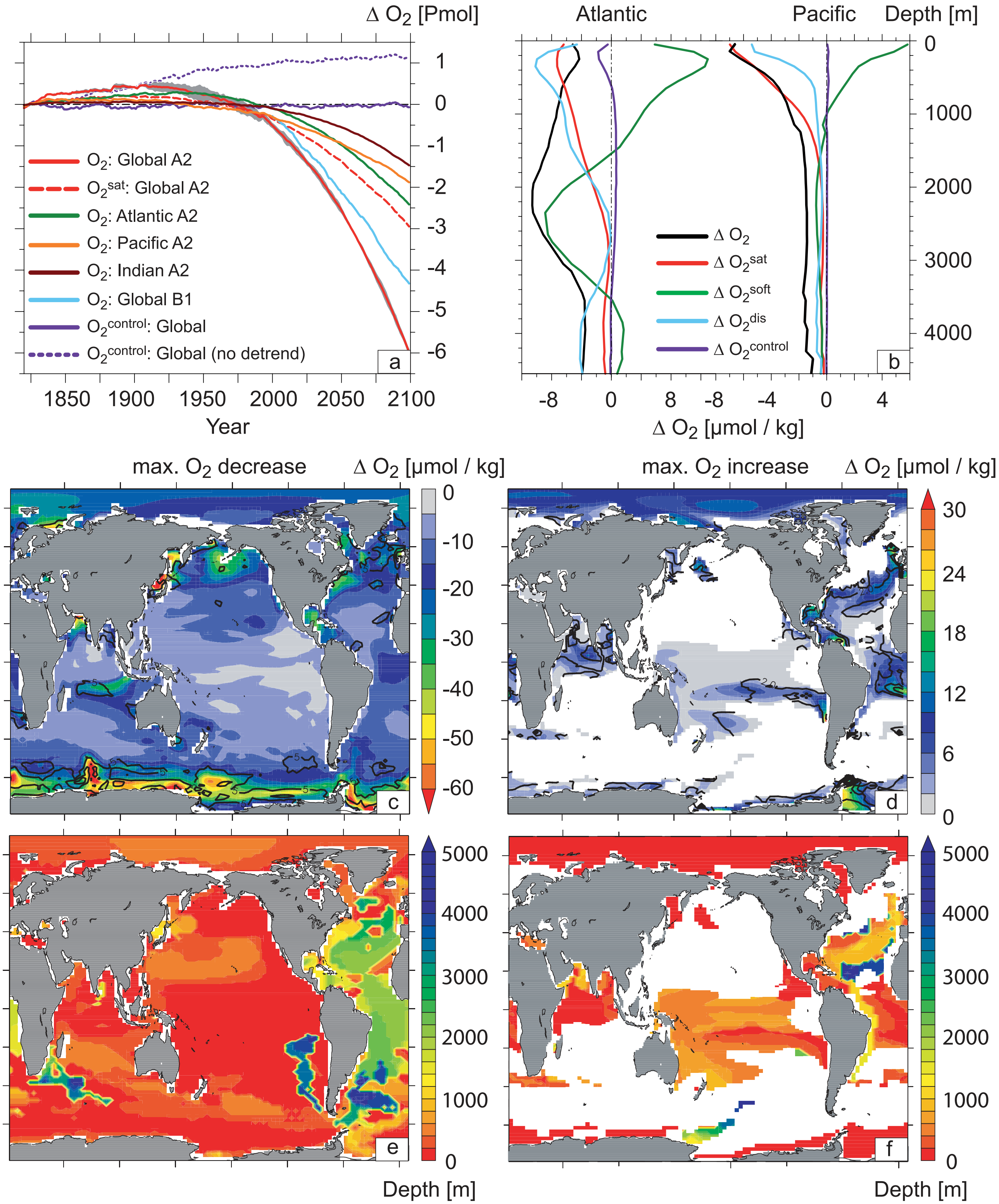
Δ O2 [Pmol]
1
0
-1
-2
-3
-4
-5
-6
O2: Global A2
O2sat: Global A2
O2: Atlantic A2
O2: Pacific A2
O2: Indian A2
O2: Global B1
O2control: Global
O2control: Global (no detrend)
a
1850 1900 1950 2000 2050 2100
Year
Atlantic
Pacific
Depth [m]
0
1000
2000
3000
4000
Δ O2
Δ O2sat
Δ O2soft
Δ O2dis
Δ O2control
b
-8 0 8 -8 -4 0 4
Δ O2 [μmol / kg]
max. O2 decrease
Δ O2 [μmol / kg]
0
-10
-20
-30
-40
-50
-60
c
max. O2 increase
Δ O2 [μmol / kg]
30
24
18
12
6
0
d
5000
4000
3000
2000
1000
0
e
Depth [m]
5000
4000
3000
2000
1000
0
f
Depth [m]

Figure 2

over the simulated period are calculated as the difference between 2090–2099 and 1820–1829, and the error bars are determined from one standard deviation among the six ensemble members. The modeled evolution of atmospheric $CO_2$ agrees within 8 ppm with $CO_2$ measurements from ice cores and atmospheric samples. By 2100, atmospheric $CO_2$ is 840 ppm and 538 ppm for the A2 scenario and the B1 scenario, respectively, comparable to other studies [*Friedlingstein et al.*, 2006].

[17] The ensemble mean global surface temperature increase from 1850–1855 to 2000–2005 of 0.81 ± 0.08°C agrees with the observation-based estimates of 0.75 ± 0.13°C [*Brohan et al.*, 2006]. The projected increase from 1990–1999 to 2090–2099 is 2.30 ± 0.04°C and 1.10 °C for the A2 and B1 scenario, respectively, reflecting the model's low transient climate response [*Friedlingstein et al.*, 2006; *Meehl et al.*, 2000].

[18] The simulated strength of the Atlantic Meridional Overturning Circulation (AMOC; maximum in the North Atlantic stream function from 20°N to 50°N and 500 m to 2000 m depth) at present of 23.1 ± 1.7 Sv is at the upper range of the observation-based estimate of 18.7 ± 5.6 Sv [*Cunningham et al.*, 2007]. AMOC is projected to decrease over the simulated period by 27% (6.7 Sv) for the A2 scenario and by 17% (4.1 Sv) for the B1 scenario, comparable to the AMOC decrease reported by *Schneider et al.* [2007] using a series of coupled AOGCM's. The upper ocean stratification, calculated as the density difference between 200 m water depth and sea surface, increases globally by 15.2% over the simulated period for the A2 scenario. Generally, the oceanic ventilation is reduced.

[19] The model projects a global decline in the export of particulate organic carbon (POC) export over the simulated period of 7% (0.63 ± 0.06 GtC $a^{-1}$) for the A2 scenario. The results show increases in POC export in the North Pacific, little change in the tropical ocean and the southern ocean and relatively large decreases in the North Atlantic and in the Indian Ocean. A detailed analysis of the present-day simulated productivity and spatiotemporal variability in the NCAR CSM1.4-carbon can be found in the work by *Schneider et al.* [2008].

[20] A global net sea-to-air oxygen flux is simulated over the historical period and the 21st century with substantial interannual to decadal variability. The model simulates an outgassing of 0.10 ± 0.06 mol $m^{-2}$ $a^{-1}$ for the year 2000 and projects an outgassing for the A2 scenario of 0.23 ± 0.10 mol $m^{-2}$ $a^{-1}$ in year 2100 (both offset corrected). This outgassing is smaller than the projected year 2100 values of 0.35 mol $m^{-2}$ $a^{-1}$ and 0.40 mol $m^{-2}$ $a^{-1}$ simulated by *Bopp et al.* [2002] and *Matear et al.* [2000], respectively, probably because of the lower transient climate response of the CSM1.4-carbon. The modeled long-term trend of the sea-to-air gas flux is reversed after explosive volcanic eruptions causing a short-term oceanic $O_2$ uptake consistent with the earlier findings by *Plattner et al.* [2002] using a simpler climate model.

[21] In summary, the global analysis suggests a significant warming of the ocean and a decreasing trend of ocean ventilation which both tend to lower oceanic $O_2$, as well as a decreasing trend of organic matter production, export and remineralization, which tend to increase subsurface $O_2$ and to decrease $O_2$ production in the surface. Globally, the ocean is losing oxygen to the atmosphere in the NCAR CSM1.4-carbon in line with recent modeling studies.

### 3.2. Variability in Dissolved Oxygen

#### 3.2.1. Anthropogenic Century-Scale Changes

[22] The total oxygen content of the global ocean is projected to decrease by 5.9 ± 0.1 Pmol (2.6%) and 4.3 Pmol (1.8%) from 1820 to 2100 for the A2 and B1 scenario, respectively (Figure 2a). The projected reduction is strongest in the Atlantic Ocean basin with 2.4 Pmol (3.7%) in comparison with the Indian Ocean with 1.5 Pmol (3.1%) and the Pacific Ocean with 1.7 Pmol (1.6%) for the A2 scenario. Because internal variability and model drift on a global scale are significantly lower than the simulated global decrease (Figure 2a), the projected decrease is almost entirely driven by anthropogenic forcing. The decrease over the 21st century is largest in shallow subsurface waters in the Pacific Ocean, whereas the maximum decrease in the Atlantic Ocean is located at a depth of 2000 m to 2500 m (Figure 2b).

[23] Turning to mechanisms, the change in the global oceanic inventory of $O_2^{sat}$ suggests that solubility-driven changes are responsible for at least 50% (2.9 Pmol) of the total decrease (Figure 2a). Global ocean inventory of $O_2^{soft}$ does not change as the phosphate inventory is conserved. In the thermocline of the Atlantic and Pacific, the $O_2$ decline is driven by solubility changes ($O_2^{sat}$) and AOU gas exchange ($O_2^{dis}$), whereas changes in $O_2^{soft}$ tend to increase oxygen concentration (Figure 2b). In the deep Atlantic (>2000 m), the term $O_2^{soft}$ dominates the simulated $O_2$ decrease. $O_2^{soft}$ decreases in response to reduced ventilation and ongoing oxygen consumption by organic matter remineralization. In other words, the vertical profile of $O_2^{soft}$ reflects a more efficient $PO_4$ utilization at the surface and additional storage of $PO_4$ in the deep caused by a slowed surface-to-deep water exchange.

[24] Projected changes in dissolved oxygen show distinct regional patterns (Figures 2c–2f). Regions with a large local decrease in dissolved oxygen are in shallow water (above 500 m) around Antarctica, in the North Pacific, in the Arabian and Japan Sea, but in intermediate water (2000–

**Figure 2.** (a) Evolution of simulated ensemble mean $O_2$ inventory anomalies over the historical period and over the 21st century relative to the 1820–1829 period. The gray shaded band denotes one standard deviation among the ensemble members. (b) Changes in the vertical distribution of $O_2$ over the 21st century (difference between 2090–2099 and 1990–1999) for the Atlantic (left) and the Pacific Ocean (right). (c–f) Spatial maps of the local maximum decrease (Figure 2c) and increase (Figure 2d) in ensemble mean dissolved oxygen within the water column over the 21st century ((2090–2099)–(1990–1999)) and the depth of the related grid cells (Figures 2e and 2f). Contours are every 5 $\mu$mol $kg^{-1}$ (Figure 2c) and every 2 $\mu$mol $kg^{-1}$ (Figure 2d) and denote one standard deviation among the ensemble members.

3000 m) in the Caribbean Sea and at the eastern coast of North America (Figures 2c and 2e). Although the average oxygen concentration is projected to decrease over the 21st century, oxygen is projected to increase at some specific locations, mainly in low latitudes in the upper ocean (Figures 2d and 2f). Increase in $O_2^{soft}$ overcompensates the decrease in $O_2^{dis}$ and $O_2^{sat}$ in this region. This increase in $O_2^{soft}$ appears primarily driven by a decrease in the export production and the consumption of $O_2$ and less by change in water mass age. We note that *Gnanadesikan et al.* [2007] find a reduction in water mass age in the tropical ocean in their model. The oxygen concentration is simulated to increase most in the Weddell Sea in shallow water by up to 25 $\mu$mol kg$^{-1}$ because of reduced sea ice and enhanced air-to-sea oxygen flux.

[25] Qualitatively, these results confirm the findings of earlier studies using less comprehensive models [*Schmittner et al.*, 2008; *Matear and Hirst*, 2003; *Bopp et al.*, 2002; *Plattner et al.*, 2002]. In general, the projected global averaged $O_2$ decrease in the NCAR model of 4.3 $\mu$mol kg$^{-1}$ from 1820 to 2100 is smaller than found in other studies (6 – 12 $\mu$mol kg$^{-1}$), probably caused by the low climate sensitivity of the model and by the inclusion of volcanoes over the historical period (see section 3.2.3). There are numerous quantitative and regional differences between the different models, which mainly depend on the representation of the biological cycle and circulation and their sensitivity to climate change.

### 3.2.2. Internal Variability

[26] We quantify local internal interannual to decadal-scale variability in $O_2$ at different depths (Figures 3a and 3b). The standard deviation of annual mean $O_2$ from the 480-year control run gives a numerically stable estimate of the variability that can be expected from internally generated climate variability, essentially the chaotic component of the climate system.

[27] The local internal variability in $O_2$ is large in high latitudes at the surface of the North Atlantic and North Pacific (Figure 3a). The variability reaches a maximum of 22 $\mu$mol kg$^{-1}$ and 9 $\mu$mol kg$^{-1}$ in subsurface water in the subpolar North Atlantic and North Pacific, respectively (Figure 3b). In particular, the standard deviation is large at depth in regions with deep water formation consistent with findings by *Levine et al.* [2008] analyzing DIC variability. The internal variability is smaller in middle and low latitudes and at larger depths. The maximum variability in AOU in the North Atlantic subsurface water is slightly smaller than in $O_2$ (not shown). This implies that the subsurface $O_2$ variability is mostly not solubility driven.

[28] Next, the internal variability in $O_2$ in the North Atlantic and the North Pacific is investigated (boxes defined by dashed lines in Figure 3a), addressing the role of NAO and PDO (see section 4 of the auxiliary material for a detailed description of the indices). The NAO is the primary source of climate variability on interannual to decadal time scales over the North Atlantic region. Observations show that the positive phase of the NAO causes a strengthening of the surface westerly winds across the Atlantic Ocean with associated warm SST anomalies in the western subtropical gyre, and cold SST anomalies in the Labrador Sea. Surface winter $O_2$ shows a significant positive correlation with simulated NAO in the northwestern subpolar gyre ($r^2$ = 0.2, n = 480) and a significant negatively correlation in the western subtropical gyre ($r^2$ = 0.1, n = 480) (Figure 3c). Simulated regression slopes often exceed 5 $\mu$mol kg$^{-1}$ per standard deviation in NAO in the northwestern subpolar gyre. Simulated winter $O_2$ is strongly negative correlated in subsurface water in the subtropical gyre ($r^2$ = 0.3, n = 480) with regression slopes of up to 5 $\mu$mol kg$^{-1}$ per NAO standard deviation (Figure 3d). The NAO-driven variability accounts for about 30% of the total variability in surface and subsurface subpolar and subtropical waters in the North Atlantic.

[29] Variations in the Pacific Ocean are linked to the PDO. Observations show that PDO causes an intensification of the westerlies over the central North Pacific, which leads to a cooling over much of the subpolar central and western Pacific and a warming in the eastern North Pacific. The model shows a significant positive correlation in the surface subpolar gyre of the North Pacific between PDO and $O_2$ ($r^2$ = 0.5, n = 480) and regression slopes of up to 5 $\mu$mol kg$^{-1}$ per standard deviation in PDO (Figure 3e). The results imply that the $O_2$ variability is entirely driven by PDO changes at the surface. The modeled regression (up to 3.5 $\mu$mol kg$^{-1}$) and correlation ($r^2$ = 0.3, n = 480) are smaller at subsurface water.

[30] The interplay of air-sea gas exchange, circulation, and the marine biological cycle and its linkages to NAO and PDO are complex and have varying impacts on $O_2$ and on regression slopes across regions and with depth. For example, NAO related regression slopes are larger at 322 m than at the surface in the subtropical North Atlantic gyre, whereas PDO related regression slopes are smaller at depth than at the surface in the less well ventilated North Pacific. A complete analysis of the resulting pattern is beyond the scope of this paper. However, the decomposition of the individual contributions to the surface $O_2$ regression slopes reveals positive contributions from variations in $O_2$ solubility ($O_2^{sat}$) and AOU gas exchange ($O_2^{dis}$) in the North Atlantic subpolar gyre, partly compensated by variations in $O_2^{soft}$. Reduced temperature in the subpolar gyre associated with a positive NAO phase enhances solubility and air-to-sea $O_2$ flux. In the North Atlantic subsurface waters, the largest contribution to the total $O_2$ regression slopes originates from variations in $O_2^{sat}$. The results may depend on the model applied and the analysis in the North Pacific should be viewed with caution as there are significant deficiencies in the simulated $O_2$ field in this region because of errors in the physical circulation and biological cycle (see section 2 in the auxiliary material). Nevertheless, the analysis shows that internal climate modes can substantially contribute to natural interannual to decadal $O_2$ variability and have to be taken into account when analyzing observed $O_2$ changes (see section 3.3).

### 3.2.3. Externally Forced Variability From Volcanic Eruptions

[31] First, the volcanic $O_2$ signal is identified by subtracting results from three pairs of simulations with and without volcanic forcing over the years 1955 to 2000 and calculating the ensemble average and standard deviation of the differences following the approach of *Church et al.* [2005]

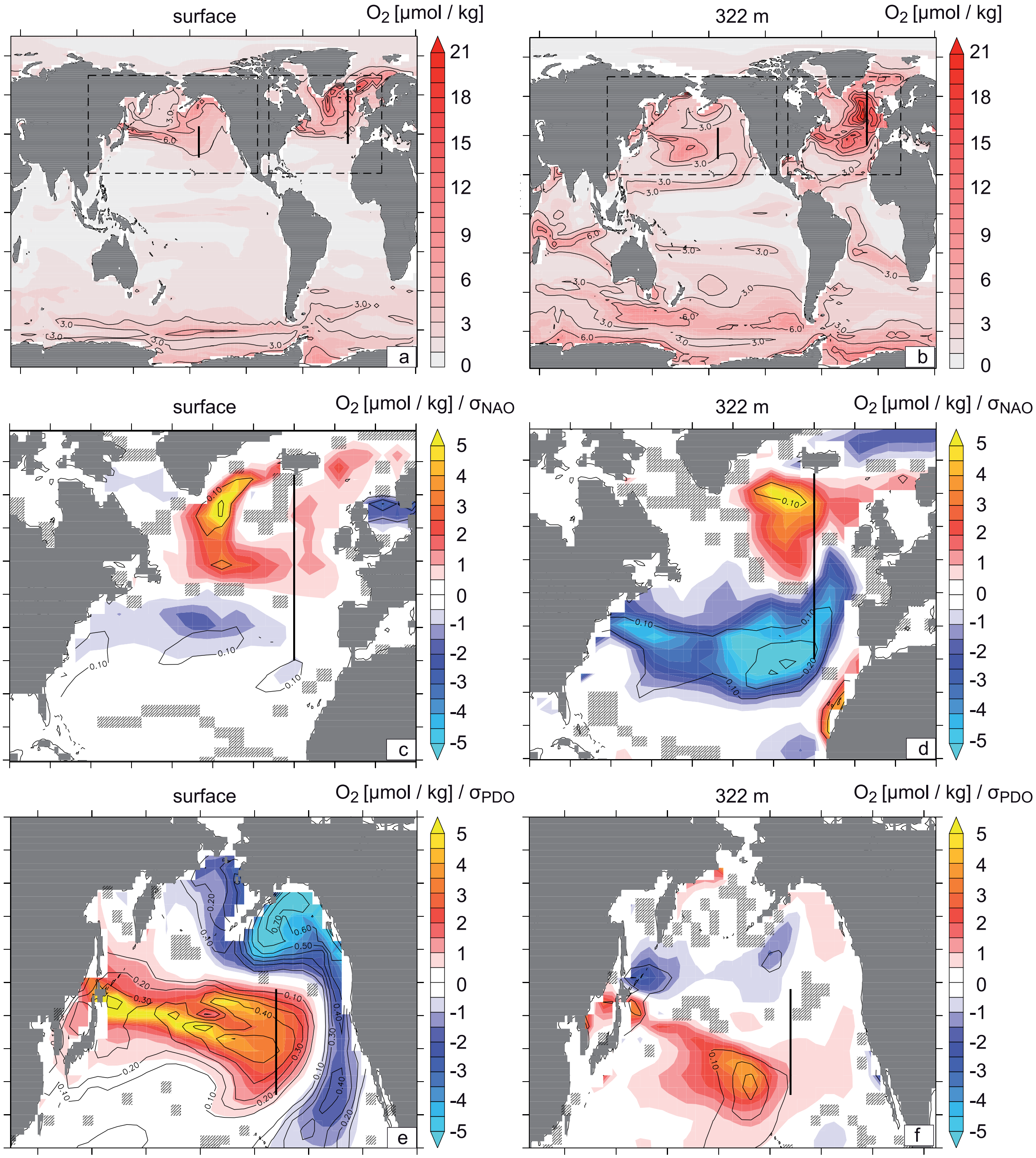

**Figure 3.** Internal variability in $O_2$, displayed as one standard deviation of annual mean $O_2$ from the control simulation, (a) at surface and (b) at 325 m depth. Contours are every 3 $\mu$mol kg$^{-1}$ and dashed lines show the two areas for Figures 3c–3d and 3e–3f, respectively. Regression of winter mean (October–March) and annual mean $O_2$ from the control simulation with the standardized annual NAO (Figures 3c and 3d) and PDO (Figures 3e and 3f) index, respectively, at (c and e) the surface and at (d and f) 322 m depth. Regression slopes correspond to one standard deviation change in the NAO and PDO index, respectively. Contour lines denote the respective squared correlation coefficients and areas without shading show statistically significant areas (*t* test, p value < 0.05). Solid thick lines show the World Ocean Circulation Experiment (WOCE) A16N and WOCE P16N section.

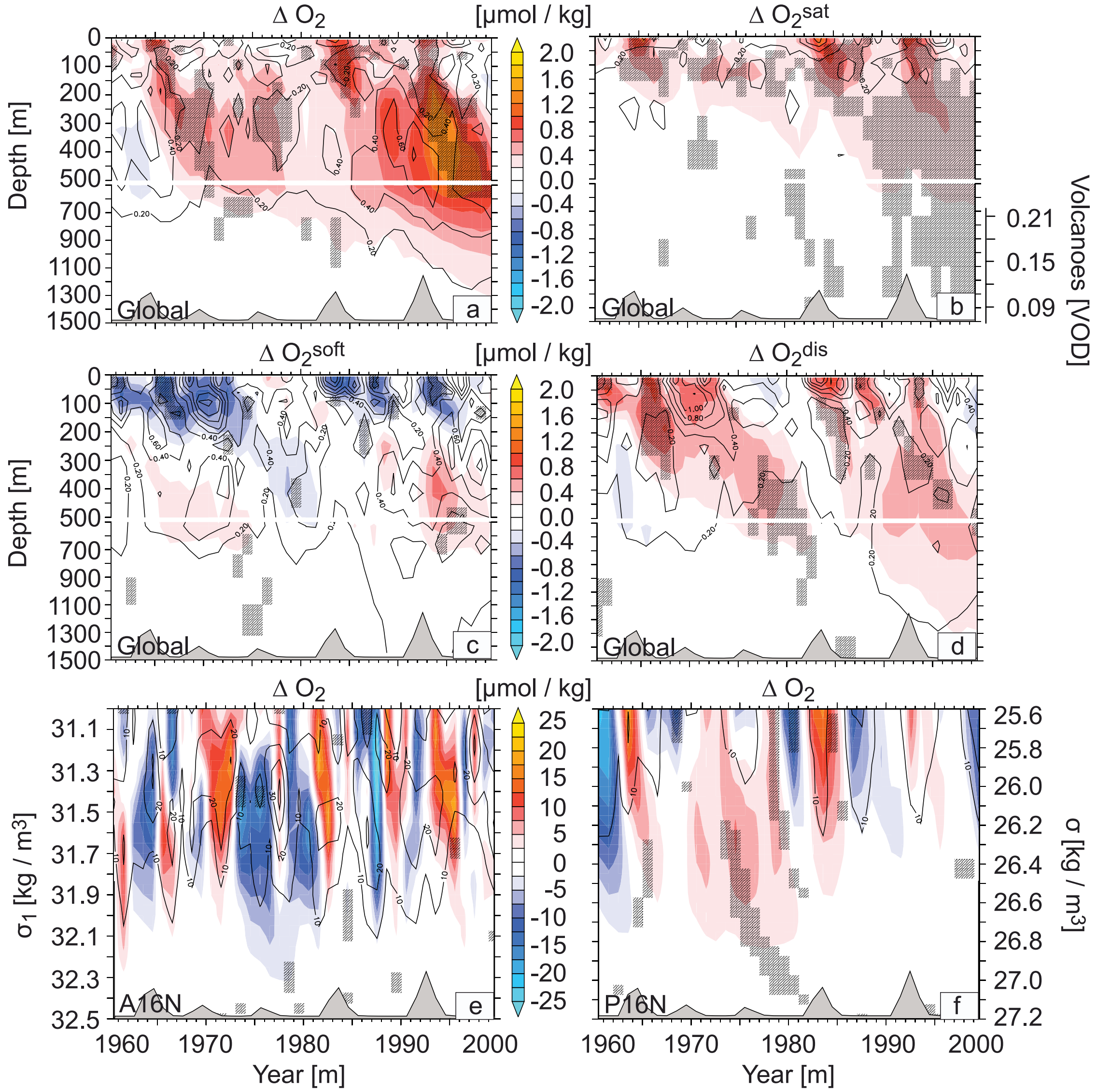

**Figure 4.** Hovmöller diagrams show the response of averaged (a) $O_2$, (b) $O_2^{sat}$, (c) $O_2^{soft}$, and (d) $O_2^{dis}$ anomalies to external volcanic forcing, as indicated by the differences between the pairs of the three ensemble simulations, over the period 1960 to 2005 globally (Figures 4a–4d), along the (e) WOCE A16N (20°W; averaged from 35°N to 65°N) and (f) WOCE P16N sections (152°W; averaged from 28°N to 44°N). Contours denote one standard deviation among the ensemble member differences and are every 0.2 $\mu$mol kg$^{-1}$ (Figures 4a–4d) and every 10 $\mu$mol kg$^{-1}$ (Figures 4e and 4f), respectively. Shaded areas mark statistically significant areas (*t* test, p value < 0.05). The radiative influence of volcanic eruptions expressed as changes in the visible optical depth are highlighted in gray on the bottom axis.

for sea level and ocean heat content. Note that removing the long-term anthropogenic trend from the standard six-member ensemble yields the same results.

[32] Figure 4a shows a Hovmöller diagram of globally averaged $O_2$ concentration anomalies from 0 to 1500 m between 1960 and 2000. During this period five explosive volcanic eruptions occurred three of which were major: Mt. Agung in year 1963, El Chichon in year 1982, and Mt. Pinatubo in year 1991. The volcanic forcing leads to a globally averaged increase in $O_2$ of about 0.4 $\mu$mol kg$^{-1}$ in the upper 1500 meters between 1955 and 2000. This increase forced by five volcanic eruptions offsets part of the decreasing trend in $O_2$ because of anthropogenic forcing over this period. Following each eruption, the model exhibits an increase in global-averaged surface $O_2$ and the signal gradually penetrates into deeper layers to about 500 m. The magnitude of the signal depends on the intensity of the eruption and the recovery in deeper layers takes up to a decade, depending on the amount of previous eruptions and

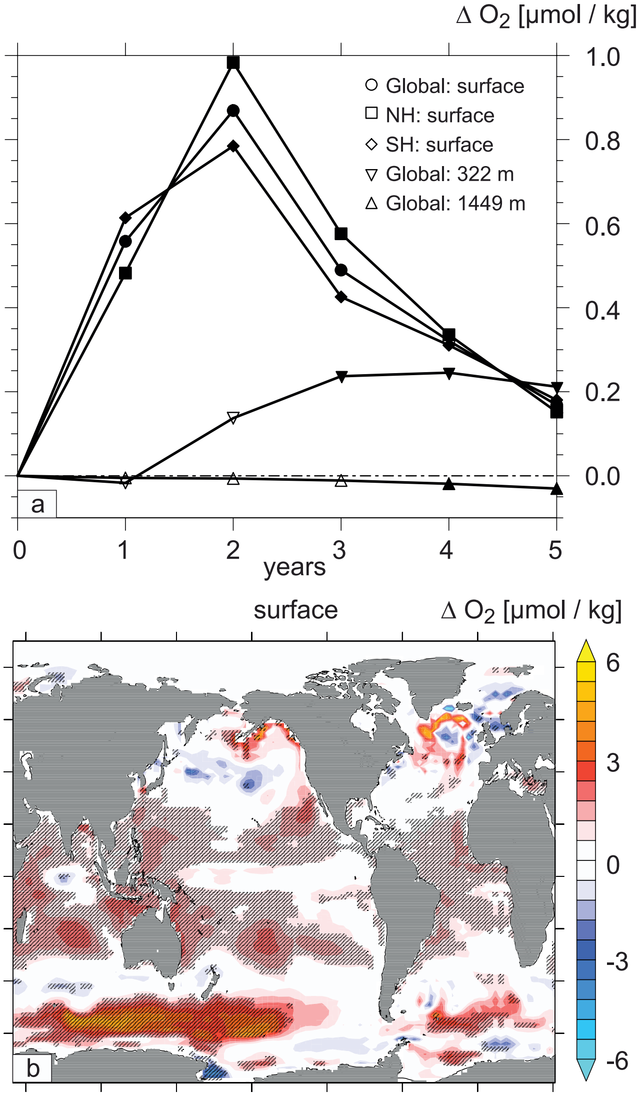

**Figure 5.** (a) Composite mean response of $O_2$ to 30 volcanic eruptions. Starting month of volcanic forcing is defined as zero. Solid and open symbols represent statistically significant and nonsignificant values, respectively (*t* test, p value < 0.05). (b) Composite mean pattern of surface $O_2$ anomalies in the first winter (October–March) following the volcanic eruptions. Shading indicates statistical significance (*t* test, p value < 0.05).

on the overlaid anthropogenically forcing [*Gleckler et al.*, 2006].

[33] The primary driver of the $O_2$ increase in the top 200 m after a volcanic eruption is the decrease of the sea surface temperature (by 0.2°C globally averaged 2 years after the beginning of a major eruption), which increases $O_2$ because of an increase in solubility as evidenced by $O_2^{sat}$ (Figure 4b). This leads to an associated increase in ventilation and higher phosphate concentrations in the surface ocean and less phosphate in the thermocline as indicated by the decrease in $O_2^{soft}$ in the top 200 m and a corresponding increase below (Figure 4c). The positive anomalies in $O_2^{dis}$ developing after a volcanic eruption penetrate from the surface into the main thermocline and reach depths of 500 m and more (Figure 4d). The decrease in $O_2^{soft}$ partly counteracts the increase in $O_2^{dis}$ and $O_2^{sat}$ in the top 200 m. In contrast, $O_2^{sat}$, $O_2^{dis}$, and $O_2^{soft}$ act in concert to elevate $O_2$ in deeper layers. Interestingly, the largest global mean $O_2$ changes for the period 1960 to 2005 are simulated at around 400 m in the late nineties and appear to reflect the cumulative impact from several earlier eruptions (Figure 4a).

[34] The oceanic $O_2$ increase due to a volcanic eruption is difficult to detect on local scale because of large unforced variability (Figures 4e and 4f). For example, we did not find a statistically significant link between $O_2$ changes and volcanic forcing along the World Ocean Circulation Experiment (WOCE) A16N section in the North Atlantic and the WOCE P16N section in the North Pacific.

[35] To investigate the mean signature of a major volcanic eruption, composites of the anomalies at different depths following the five largest low-latitude eruptions beginning with Krakatoa in year 1883 of all six ensemble members were made. We have defined the anomalies in the 5 postvolcano years relative to a −1 year preeruption period. The use of anomalies provides a volcanic signal without overlaying long-term trends and without integrating effects from preeruptions as visible in Figure 4a. Only 5 postvolcanic years were included in order to avoid direct overlap with later eruptions. A major tropical volcanic eruption leads to a significant globally averaged $O_2$ increase of 0.9 $\mu mol\,kg^{-1}$ at the surface and an increase of 0.3 $\mu mol\,kg^{-1}$ at 322 m depth 2 and 3 years after the explosion, respectively (Figure 5a). The globally averaged $O_2$ increase is slightly larger in the Northern than in the Southern Hemisphere. Subsurface water shows a delayed response of 1 year to a volcanic eruption. The volcanic signals disappear with larger depth.

[36] Figure 5b shows averaged $O_2$ composites response to 30 volcanic eruptions in the first winter period (October–March) at the surface. Overall, there is a lack of statistical significance on local scales at high latitudes, indicating a large spread of responses among the ensemble members, although the volcanic forcing is higher at high latitudes. Volcanic eruptions lead to a partly significant increase in $O_2$ at the surface in the low-latitude Pacific Ocean and in the southern ocean (Figure 5b). Almost no locally significant changes in $O_2$ occur in subsurface water (not shown). A significant positive phase of the NAO in response to volcanic forcing has been found in observations [*Fischer et al.*, 2007] and is often used to evaluate the volcanic responses in simulations [*Stenchikov et al.*, 2006]. The NCAR CSM1.4 model shows a tendency to a NAO-like pattern in atmospheric pressure and temperature in the first winter after a major low-latitude volcanic eruption. However, the changes are not significantly distinct from zero. This is possibly related to the coarse vertical resolution in the stratosphere and/or insufficient coupling between volcanic forcing, stratospheric wave action and the atmospheric circulation at the surface.

[37] Quantifying the impacts of volcanic eruptions, which are newly implemented in the model, is important to understand oxygen variability and provides hints for the

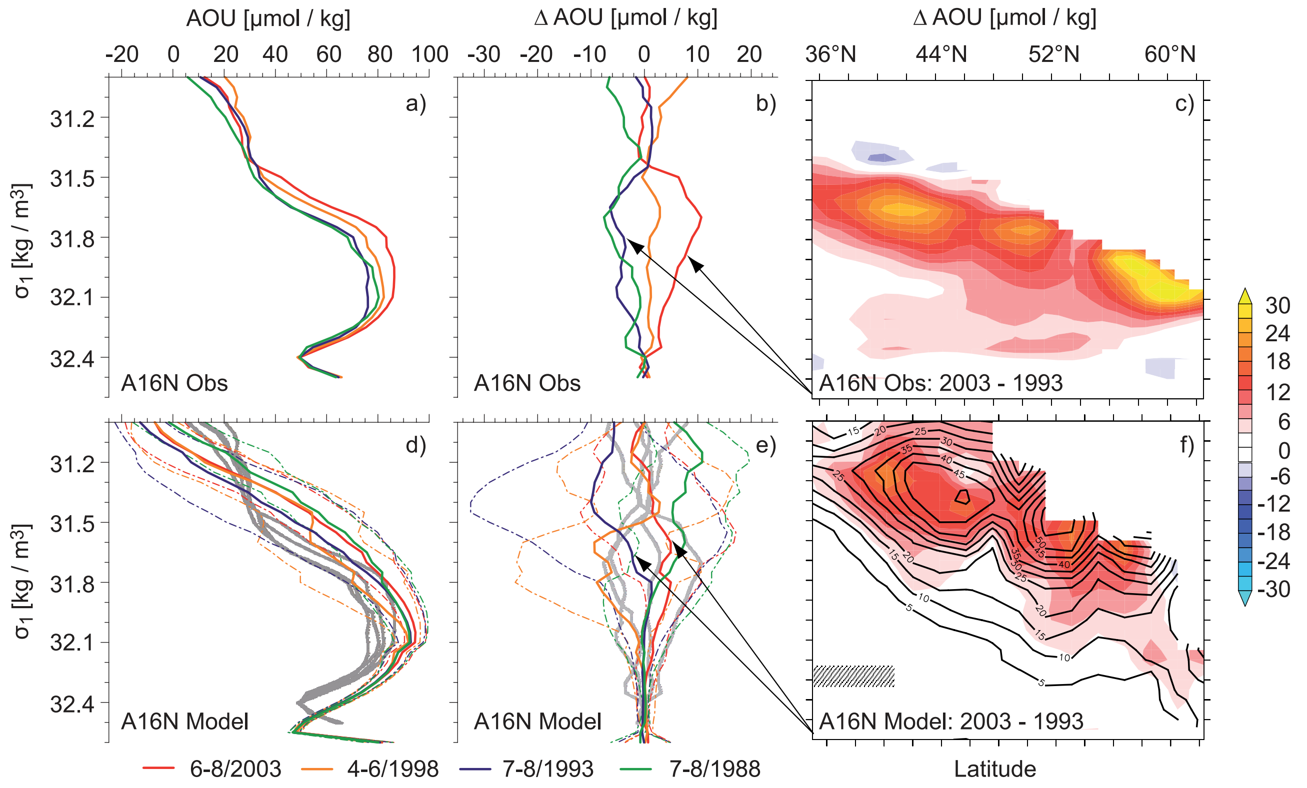

**Figure 6.** (a) Observed and (d) modeled AOU along A16N on different density layers for different years. Month and year of sampling are indicated by the labels. (b and e) $\Delta$AOU represents the difference relative to the mean from all cruises. Dotted lines represent one standard deviation among the six ensemble members and the gray lines show the observations for comparison. Section A16N is along 20°W, and data are averaged from 35°N to 63°N. (c) Data-based versus (f) modeled AOU changes from 1993 to 2003. Contours at 5 $\mu$mol kg$^{-1}$ intervals indicate one standard deviation among the ensemble differences, and shaded areas mark statistically significant simulated changes (*t* test, p value $< 0.05$). Data within the seasonal pycnocline are marked out. The observed seasonal pycnocline is calculated with data from WOA01 [*Conkright et al.*, 2002]. Additional details about the observational data used here for illustrative model data comparison and about the interpolation method can be found in section 5 of the auxiliary material.

interpretation of observational records (see section 3.3). We conclude that major volcanic eruptions have to be included in the interpretation of oxygen variability. The impact of a single volcanic eruption on the oxygen concentration is largest at the surface and tends to decrease with depth. Regional changes in oxygen due to volcanic eruptions are difficult to detect, especially at high latitudes, because of the low signal (volcano) to noise (internal variability) ratio. The model indicates a tendency for the North Atlantic oxygen to be represented in the high NAO index state after a volcanic eruption.

### 3.3. Interdecadal Changes in Dissolved Oxygen: Model Versus Observations

[38] We further investigate the ability of the model to represent observed interdecadal dissolved oxygen changes and if the simulated internal natural variability (one standard deviation among the six ensemble simulations) masks some of the projected long-term trends over the observational period. We compare observed AOU differences between cruises along similar transects over the last 20 to 30 years in the North Atlantic (A16N) and the North Pacific (P16N) to modeled AOU changes for the same transects and periods and to the associated simulated ensemble spread (see section 5 in the auxiliary material for additional details about the observational data used here). Note that the simulated AOU depth profiles are not expected to fit a specific year, because fully coupled carbon cycle–climate models as used in the current study generate their own internal climate variability.

[39] The focus here is on four cruises in the eastern part of the subpolar gyre in the North Atlantic Ocean between 35°N and Iceland (63°N) along 20°W from 1988 to 2003. Observed water property changes along this section are investigated in detail by *Johnson and Gruber* [2007]. The model represents the main features in AOU found in the observations (Figures 6a and 6d). The low AOU concentration in the well-ventilated Subpolar Mode Water, just below

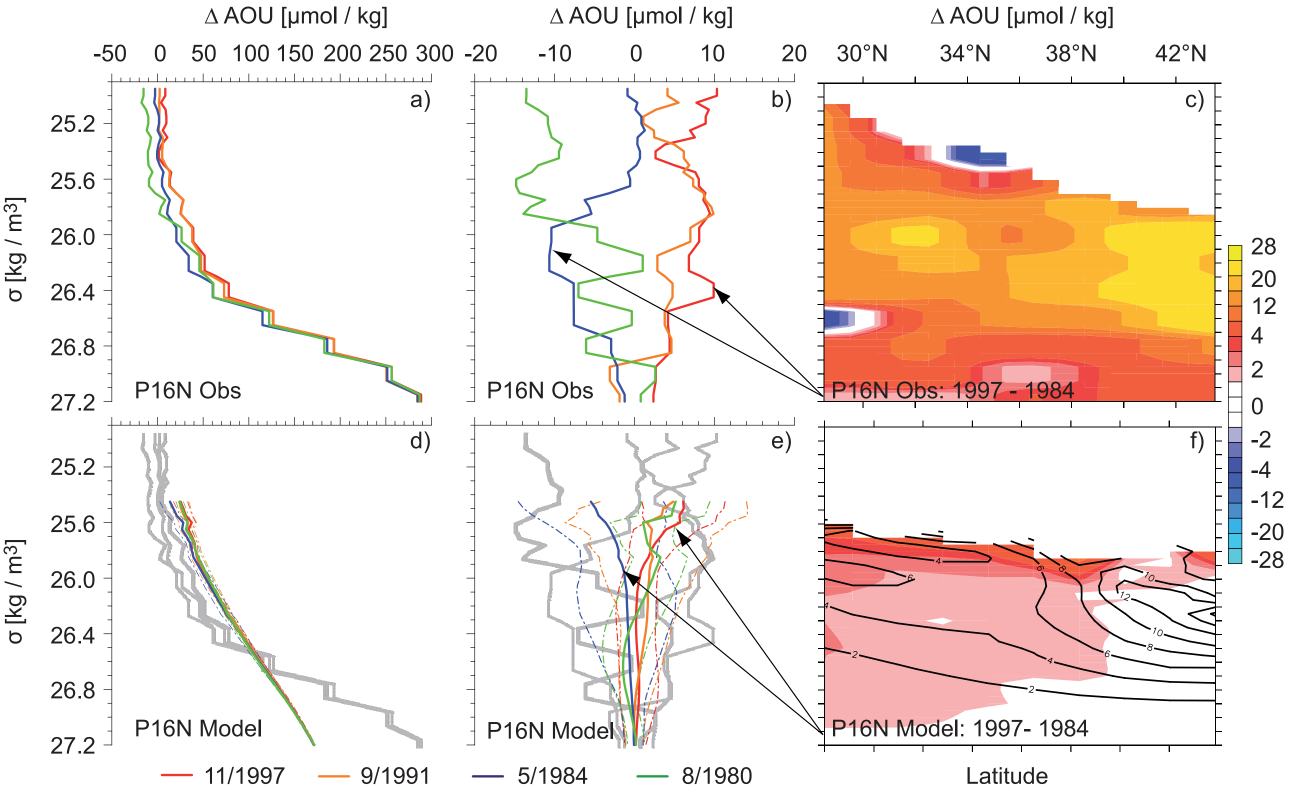

**Figure 7.** Following Figure 6 except for the North Pacific along 152°W from 28°N to 44°N.

the seasonal pycnocline, is slightly underestimated by the model, because of a simulated cold bias compared with observations. The AOU maximum around $\sigma_1 = 32$ kg m$^{-3}$ is slightly overestimated (by up to 10 $\mu$mol kg$^{-1}$) in the model, implying a lower ventilation rate or differences in remineralization processes (related to differences in surface production and export) in the model.

[40] Turning to decadal-scale variability (Figures 6b and 6e) the simulated variability in the ensemble mean for the 4 cruises is comparable to the observed variability and the standard deviation among the ensemble member (internal variability) for a specific year reaches up to 20 $\mu$mol kg$^{-1}$ on $\sigma_1 = 31.3$ kg m$^{-3}$. Generally, observations show increases in AOU from the late 1980s to the earliest 2000s within the permanent pycnocline (as indicated with arrows in Figure 6b). To investigate this observed trend, we analyze spatially simulated differences between 2003 and 1993 in AOU (Figures 6c and 6f). These two sections were occupied in nearly the same months, thus seasonal biases should be small. Observed AOU locally increases by up to 35 $\mu$mol kg$^{-1}$ near Iceland and around 42°N and 50°N, just below the seasonal pycnocline (Figure 6c). The ensemble mean shows an increase in AOU in the upper water by up to 20 $\mu$mol kg$^{-1}$ (Figure 6f), but the increase is not statistically significant, because the ensemble range yields large variability in the 2003–1993 AOU difference throughout the upper ocean. The standard deviation of the ensemble members reaches up to 45–50 $\mu$mol kg$^{-1}$ for the 2003–1993 difference in regions where the largest ensemble mean increase of 20 $\mu$mol kg$^{-1}$ in AOU is simulated. The volcanic eruption of the Mt. Pinatubo in year 1991 has no statistically significant influence on the local AOU changes (Figure 4e).

### 3.3.1. North Pacific: P16N

[41] Changes in dissolved oxygen in the North Pacific have been extensively analyzed and documented [*Deutsch et al.*, 2006; *Emerson et al.*, 2004]. Data from three sections in the North Pacific show large, but spatially and temporally complex $O_2$ changes over the last decades [*Deutsch et al.*, 2006]. Here we focus on four cruises along 152°W between 28°N to 44°N from the early 1980s to the late 1990s.

[42] The observed AOU increase with depth is much sharper than simulated by the model (Figures 7a and 7d), and the AOU concentration on denser sigma levels is generally underestimated in the model because of too low export of organic matter and deficiencies in modeled circulation. The simulated pycnocline is on higher density levels and denser water masses outcrop in the model in the observations.

[43] The ensemble mean AOU changes are smaller than observed (Figures 7b and 7e). However, the simulated variability (ensemble spread) reaches up to 10 $\mu$mol kg$^{-1}$ on lighter sigma levels comparable to the observed AOU anomalies. At larger depth, the model underestimates the observed variability.

[44] Observations show lower AOU concentrations in 1980 and 1984, than in 1991 and 1997 (Figure 7b). For illustration, we discuss AOU differences between 1997 and

1984 (Figures 7c and 7f). The observed AOU differences between the two cruises are almost everywhere positive (Figure 7c) and greater at higher latitudes. The observed AOU increase on the order of 20–35 $\mu$mol kg$^{-1}$ in the subarctic ocean is centered between $\sigma_0$ = 25.9 kg m$^{-3}$ and $\sigma_0$ = 26.8 kg m$^{-3}$. The model has a similar feature of increasing AOU, but the model underestimates the magnitude found from observations (Figure 7f). The variability of AOU among the ensemble members is largest at the northern edge of the transect and reaches up to 14 $\mu$mol kg$^{-1}$. The simulated AOU increase is nowhere statistically significant.

### 3.3.2. Synthesis

[45] The analysis indicates that the simulated decadal-scale variability in AOU in the North Atlantic and Pacific is comparable to observation-based estimates. The model is able to represent the pattern of changes within the variations among ensemble members and the large spread of the model ensemble suggests that most of the variability may be explained by internal variations. High-frequency variability (seasonal or shorter) likely contributes locally to the observed $O_2$ differences between repeated cruises. However, overall changes in AOU averaged along the cruises analyzed here are hardly affected by seasonal variations in our analysis. Further, we have used corresponding monthly output to compare model results with observations. Errors in oxygen measurements for all cruises are on the order of 1–5 $\mu$mol kg$^{-1}$ and cannot account for the large variability found along the investigated sections.

[46] The simulated local (grid cell) $O_2$ variability along A16N and P16N over the observational period is difficult to attribute to mechanisms as the signal-to-noise ratio decreases sharply with decreasing spatial and temporal scales. Nevertheless, the analysis of the internal variability from results of the 480-year control run (see section 3.2.2) indicates a possibly significant link between the modes like the NAO and PDO, and the oxygen concentration. The findings in the North Atlantic are consistent with the hypothesis from *Johnson and Gruber* [2007] of higher $O_2$ during positive NAO phases along the northern part of the A16N. Decadal variations in the North Pacific $O_2$ are possibly linked to the PDO. The model shows a significant positive correlation along P16N between PDO and surface $O_2$. Recent observations show that a statistically significant correlation between $O_2$ and PDO is absent along the transect P16N in subsurface waters [*Mecking et al.*, 2008], a result that is not inconsistent with our findings of much weaker correlations between $O_2$ and PDO at depths than near the surface.

## 4. Discussion and Conclusions

[47] In this study, we have investigated oceanic oxygen variations on different spatial and temporal scales using a six-member ensemble simulation from a coupled climate carbon cycle model. Different caveats have to be considered. First, our study is based on a relatively coarse resolution AOGCM. As a result, mesoscale variability, which can contribute substantially to oceanic variability and also to the mean state, is not explicitly resolved [*Haine and Gray*, 2001]. Second, the simple parametrization of the marine biological cycle may not correctly represent variability in production and remineralization of organic matter. The assumption of constant and uniform Redfield ratios used in this study may not be valid for future projections. *Oschlies et al.* [2008] suggest that changing Redfield ratios may lead to a significant increase in the volume of suboxic water in the tropical oceans in response to the respiration of excess organic carbon formed at high $CO_2$ levels. Further, the number of ensemble members used in this present study is constrained by the available computational resources. The relatively small sample of independent realizations (n = 6) provides a rather limited probability distribution of oxygen changes.

[48] Coupled carbon cycle–climate simulations are expensive to run and to analyze and decisions need to be taken how to split available CPU time and human resources between ensemble and sensitivity simulations. The focus in this study was on analyzing ensemble runs as this has been largely neglected in biogeochemical climate modeling. Ensemble simulations permit one to separate the impact of internal (unforced) variability from forced variability. The ensemble mean approximates externally forced signals, as internal variability is distributed by chance (white noise) and thus removed (or smoothed) when results from the individual ensemble members are averaged. Sensitivity simulations on the other hand are appropriate to identify and quantify individual mechanisms and processes, to explore uncertainty ranges and possible outcomes (e.g., scenarios B1 versus A2). Dedicated tracers (e.g., $O_2^{sat}$, $O_2^{soft}$, and $O_2^{dis}$) can also be used to quantify individual processes. In conclusion, both ensemble simulations and sensitivity tests are required for a comprehensive analysis.

[49] Including all relevant natural and anthropogenic forcings results in reasonable representations of decadal-scale spatiotemporal variability associated with the variability in forcing from pulse-like, short-term, volcanic cooling events and internal climate system variability. Despite caveats, the simulated changes are comparable to those observed along repeated transects in the North Atlantic (A16N) and Pacific (P16N), suggesting that the model captures key mechanisms of late 20th century $O_2$ variability.

[50] Our modeling study suggests that over recent decades internal natural variability tends to mask simulated century-scale trends in dissolved oxygen from anthropogenic forcing in the North Atlantic and Pacific. Observed changes in oxygen are similar or even smaller in magnitude than the spread of the ensemble simulation. The observed decreasing trend in dissolved oxygen in the Indian Ocean thermocline and the boundary region between the subtropical and subpolar gyres in the North Pacific has reversed in recent years [*McDonagh et al.*, 2005; *Mecking et al.*, 2008], implicitly supporting this conclusion.

[51] The presence of large-scale propagating $O_2$ anomalies, linked with major climate modes, complicates the detection of long-term trends in oceanic $O_2$ associated with anthropogenic climate change. In particular, we find a statistically significant link between $O_2$ and the dominant climate modes (NAO and PDO) in the North Atlantic and North Pacific surface and subsurface waters, which are

causing more than 50% of the total internal variability of $O_2$ in these regions.

[52] Explosive volcanic eruptions impose major perturbations to climate and marine oxygen on top of a background on internally driven climate variability. The impact of a single volcanic eruption on $O_2$ is identifiable on global scales, but difficult to detect on local scales at high latitudes. After each volcanic eruption, oxygen is taken up by the ocean and ocean oxygen inventory increases globally in the top 500 m. The perturbation persists for up to a decade after an individual eruption. On longer time scales, the $O_2$ increase due to a volcanic eruption offsets part of the decreasing trend in $O_2$ because of anthropogenic forcing, similar to the findings of *Gleckler et al.* [2006] for ocean heat content. The $O_2$ uptake is partly thermally driven; volcanic cooling increases solubility and air-to-sea $O_2$ flux. In addition, upper ocean stratification decreases and ventilation of the upper thermocline increases after volcanic eruptions, favoring a further increase in upper ocean $O_2$. Because climate projections for the 21st century and beyond neglect volcanic eruptions, current projected ocean oxygen decreases are likely overestimated to some degree. In conclusion, volcanic forcing causes considerable variability in the biogeochemical system and should be taken into account in any analysis of change.

[53] AOU variations have significant implications for estimates of the oceanic uptake of anthropogenic carbon from ocean tracer studies using empirical approaches [*Levine et al.*, 2008]. The AOU signal is used to eliminate the contribution of organic matter remineralization to the DIC concentrations. The decadal-scale observed AOU changes of up to 30 $\mu$mol kg$^{-1}$ imply DIC changes of 20.6 $\mu$mol kg$^{-1}$, when using a C:$O_2$ Redfield ratio of 117:–170. Such a DIC change is larger than the decadal increase in DIC expected in the mixed layer from the uptake of anthropogenic $CO_2$ from the atmosphere [*Johnson and Gruber*, 2007]. Thus, internal variability may significantly affect data-based reconstructions of anthropogenic carbon as recently demonstrated [*Levine et al.*, 2008].

[54] In a future warming climate, the global dissolved oxygen decrease is projected to become significant. Oxygen content decrease with global warming mainly in the Pacific Ocean and the Indian Ocean in shallow water, and in the Atlantic in intermediate water. Oxygen concentration is also projected to increase over the 21st century in low latitudes in the upper ocean because of an overcompensating effect of the reduced organic matter cycle. Reduced upwelling of deep waters under global warming and associated reduction in water age could also lead to a local increase in dissolved oxygen [*Gnanadesikan et al.*, 2007]. In the NCAR model, the deep overturning circulation is only changing significantly in the North Atlantic. This suggests that the reduced upwelling is not the reason for the $O_2$ increase. However, we imply that large interannual to decadal variations of oceanic oxygen make the detections of anthropogenic $O_2$ changes and their attribution to anthropogenic forcings currently challenging along the investigated transects in the North Pacific and North Atlantic.

[55] To date, the ability to detect and interpret observed changes is still limited by lack of data. Additional biogeochemical data from time series and profiling floats, such as the Argo array (http://www.argo.ucsd.edu) are needed to improve the detection of ocean oxygen and carbon system changes and our understanding of climate change.

[56] **Acknowledgments.** Simulations were carried out at the Swiss National Computing Centre in Manno, Switzerland. This study is supported by the EU projects CARBOOCEAN (511176-2) and EUROCEANS (511106-2) and the Swiss National Science Foundation. We would like to thank C. C. Raible for stimulating discussions. K. Bieri maintained the local computing facilities. We thank S. Emerson, C. Deutsch, G. Johnson, and N. Gruber for making data from several cruises available. Helpful comments from C. Le Quéré and two anonymous reviewers are acknowledged.

## References

Ammann, C. M., G. A. Meehl, W. M. Washington, and C. S. Zehnder (2003), A monthly and latitudinally varying volcanic forcing dataset in simulations of 20th century climate, *Geophys. Res. Lett.*, *30*(12), 1657, doi:10.1029/2003GL016875.

Ammann, C. M., F. Joos, D. S. Schimel, B. L. Otto-Bliesner, and R. A. Tomas (2007), Solar influence on climate during the past millennium: Results from transient simulations with the NCAR Climate System Model, *Proc. Natl. Acad. Sci., U. S. A.*, *104*(10), 3713–3718, doi:10.1073/pnas.0605064.

Anderson, L. A., and J. L. Sarmiento (1994), Redfield ratios of remineralization determined by nutrient data analysis, *Global Biogeochem. Cycles*, *8*, 65–80.

Andres, R. J., D. J. Fielding, G. Marland, T. A. Boden, N. Kumar, and A. T. Kearney (1999), Carbon dioxide emissions from fossil-fuel use, 1751–1950, *Tellus Ser. B*, *51*, 759–765.

Bopp, L., C. L. Quéré, M. Heimann, A. C. Manning, and P. Monfray (2002), Climate-induced oceanic oxygen fluxes: Implications for the contemporary carbon budget, *Global Biogeochem. Cycles*, *16*(2), 1022, doi:10.1029/2001GB001445.

Boville, B. A., and P. R. Gent (1998), The NCAR Climate System Model: Version one, *J. Clim.*, *11*, 1115–1130.

Boville, B. A., J. T. Kiehl, P. J. Rasch, and F. O. Bryan (2001), Improvements to the NCAR CSM-1 for transient climate simulations, *J. Clim.*, *14*, 164–179.

Brohan, P., J. J. Kennedy, I. Harris, S. F. B. Tett, and P. D. Jones (2006), Uncertainty estimates in regional and global observed temperature changes: A new dataset from 1850, *J. Geophys. Res.*, *111*, D12106, doi:10.1029/2005JD006548.

Church, J. A., N. J. White, and J. M. Arblaster (2005), Significant decadal-scale impact of volcanic eruptions on sea level and ocean heat content, *Nature*, *438*, 74–77, doi:10.1038/nature04237.

Conkright, M. E., R. A. Locarnini, H. Garcia, T. O. Brien, T. Boyer, C. Stephens, and J. Antonov (2002), *World Ocean Atlas 2001*, vol. 4, *Nutrients, NOAA Atlas NESDIS*, vol. 52, NOAA, Silver Spring, Md.

Cunningham, S. A., et al. (2007), Temporal variability of the atlantic meridional overturning circulation at 26.5°N, *Science*, *317*(5840), 935–938, doi:10.1126/science.1141304.

Deutsch, C., S. Emerson, and L. Thompson (2006), Physical-biological interactions in North Pacific oxygen variability, *J. Geophys. Res.*, *111*, C09S90, doi:10.1029/2005JC003179.

Doney, S. C., K. Lindsay, I. Fung, and J. John (2006), Natural variability in a stable, 1000-yr global coupled climate-carbon cycle simulation, *J. Clim.*, *19*, 3033–3054.

Emerson, S., Y. W. Watanabe, T. Ono, and S. Mecking (2004), Temporal trends in apparent oxygen utilization in the upper pycnocline of the North Pacific: 1980–2000, *J. Oceanogr.*, *60*, 139–147.

Fischer, E. M., J. Luterbacher, E. Zorita, S. F. B. Tett, C. Casty, and H. Wanner (2007), European climate response to tropical volcanic eruptions over the last half millennium, *Geophys. Res. Lett.*, *34*, L05707, doi:10.1029/2006GL027992.

Forster, P., et al. (2007), Changes in atmospheric constituents and in radiative forcing, in *Climate Change 2007: The Physical Science Basis: Contribution of Working Group I to the Fourth Assessment Report of the Intergovernmental Panel on Climate Change*, edited by S. Solomon et al., pp. 129–234, Cambridge Univ. Press, New York.

Friedlingstein, P., et al. (2006), Climate-carbon cycle feedback analysis: Results from the C4MIP model intercomparison, *J. Clim.*, *19*, 3337–3353.

Fung, I. Y., S. C. Doney, K. Lindsay, and J. John (2005), Evolution of carbon sinks in a changing climate, *Proc. Natl. Acad. Sci., U. S. A.*, *102*(32), 11,201–11,206, doi:10.1073/pnas.0504949102.

Garcia, H. E., R. A. Locarnini, T. P. Boyer, and J. I. Antonov (2006), *World Ocean Atlas 2005*, vol. 3, *Dissolved Oxygen, Apparent Oxygen Utilization, and Oxygen Saturation, NOAA Atlas NESDIS*, vol. 63, NOAA, Silver Spring, Md.

Gent, P. R., F. O. B. G. Danabasoglu, S. C. Doney, W. R. Holland, W. G. Large, and J. C. McWilliams (1998), The NCAR Climate System Model global ocean component, *J. Clim.*, *11*, 1287–1306.

Gleckler, P. J., K. AchutaRao, J. M. Gregory, B. D. Santer, K. E. Taylor, and T. M. L. Wigley (2006), Krakatoa lives: The effect of volcanic eruptions on ocean heat content and thermal expansion, *Geophys. Res. Lett.*, *33*, L17702, doi:10.1029/2006GL026771.

Gnanadesikan, A., J. L. Russell, and F. Zeng (2007), How does ocean ventilation change under global warming?, *Ocean Sci.*, *3*(1), 43–53.

Haine, T. W. N., and S. L. Gray (2001), Quantifying mesoscale variability in ocean transient tracer fields, *J. Geophys. Res.*, *106*, 13,861–13,878.

Houghton, R. A. (1999), The annual net flux of carbon to the atmosphere from changes in land use 1850–1990, *Tellus Ser. B*, *51*, 298–313.

Intergovernmental Panel on Climate Change (2000), *Special Report on Emissions Scenarios*, edited by N. Nakicenovic et al., 599 pp., Cambridge Univ. Press, New York.

Johnson, G. C., and N. Gruber (2007), Decadal water mass variations along 20°W in the northeastern Atlantic Ocean, *Prog. Oceanogr.*, *73*, 277–295, doi:10.1016/j.pocean.2006.03.022.

Jones, C. D., and P. M. Cox (2001), Modelling the volcanic signal in the atmospheric $CO_2$ record, *Global Biogeochem. Cycles*, *15*, 453–465.

Joos, F., M. Bruno, R. Fink, T. F. Stocker, U. Siegenthaler, C. L. Quéré, and J. L. Sarmiento (1996), An efficient and accurate representation of complex oceanic and biospheric models of anthropogenic carbon uptake, *Tellus Ser. B*, *48*, 397–417.

Joos, F., I. C. Prentice, S. Sitch, R. Meyer, G. Hooss, G.-K. Plattner, S. Gerber, and K. Hasselmann (2001), Global warming feedbacks on terrestrial carbon uptake under the Intergovernmental Panel on Climate Change IPCC emission scenarios, *Global Biogeochem. Cycles*, *15*, 891–907.

Joos, F., G.-K. Plattner, T. F. Stocker, A. Körtzinger, and D. W. R. Wallace (2003), Trends in marine dissolved oxygen: Implications for ocean circulation changes and the carbon budget, *Eos Trans. AGU*, *84*(21), 197–201.

Keller, K., R. D. Slater, M. Bender, and R. Key (2002), Possible biological or physical explanations for decadal scale trends in North Pacific nutrient concentrations and oxygen utilization, *Deep Sea Res., Part II*, *49*, 345–362.

Key, R. M., A. Kozyr, C. L. Sabine, K. Lee, R. Wanninkhof, J. Bullister, R. A. Feely, F. Millero, C. Mordy, and T.-H. Peng (2004), A global ocean carbon climatology: Results from GLODAP, *Global Biogeochem. Cycles*, *18*, GB4031, doi:10.1029/2004GB002247.

Kiehl, J. T., J. J. Hack, G. B. Bonan, B. A. Boville, D. L. Williamson, and P. J. Rasch (1998), The National Center for Atmospheric Research Community Climate Model, *J. Clim.*, *11*, 1151–1178.

Levine, N. M., S. C. Doney, R. Wanninkhof, K. Lindsay, and I. Y. Fung (2008), Impact of ocean carbon system variability on the detection of temporal increases in anthropogenic $CO_2$, *J. Geophys. Res.*, *113*, C03019, doi:10.1029/2007JC004153.

Marland, G., and R. M. Rotty (1984), Carbon dioxide emissions from fossil fuels: A procedure for estimation and results for 1950–1982, *Tellus Ser. B*, *36*, 232–261.

Matear, R. J., and A. C. Hirst (2003), Long-term changes in dissolved oxygen concentrations in the ocean caused by protracted global warming, *Global Biogeochem. Cycles*, *17*(4), 1125, doi:10.1029/2002GB001997.

Matear, R. J., A. C. Hirst, and B. I. McNeil (2000), Changes in dissolved oxygen in the Southern Ocean with climate change, *Geochem. Geophys. Geosyst.*, *1*(11), 1050, doi:10.1029/2000GC000086.

McDonagh, E. L., H. L. Bryden, B. A. King, R. J. Sanders, S. A. Cunningham, and R. Marsh (2005), Decadal changes in the south Indian Ocean thermocline, *J. Clim.*, *18*, 1575–1590.

Mecking, S., C. Langdon, R. A. Feely, C. L. Sabine, C. A. Deutsch, and D.-H. Min (2008), Climate variability in the North Pacific thermocline diagnosed from oxygen measurements: An update based on the U.S. CLIVAR/$CO_2$ Repeat Hydrography Cruises, *Global Biogeochem. Cycles*, *22*, GB3015, doi:10.1029/2007GB003101.

Meehl, G. A., W. D. Collins, B. Boville, J. T. Kiehl, T. M. L. Wigley, and J. M. Arblaster (2000), Response of the NCAR Climate System Model to increased $CO_2$ and the role of physical processes, *J. Clim.*, *13*, 1879–1898.

Meehl, G. A., et al. (2007), Global climate projections, in *Climate Change 2007: The Physical Science Basis: Contribution of Working Group I to the Fourth Assessment Report of the Intergovernmental Panel on Climate Change*, edited by S. Solomon et al., pp. 747–845, Cambridge Univ. Press, New York.

Najjar, R. G., et al. (2007), Impact of circulation on export production, dissolved organic matter, and dissolved oxygen in the ocean: Results from Phase II of the Ocean Carbon-cycle Model Intercomparison Project (OCMIP-2), *Global Biogeochem. Cycles*, *21*, GB3007, doi:10.1029/2006GB002857.

Oschlies, A., K. G. Schulz, U. Riebesell, and A. Schmittner (2008), Simulated 21st century's increase in oceanic suboxia by $CO_2$-enhanced biotic carbon export, *Global Biogeochem. Cycles*, *22*, GB4008, doi:10.1029/2007GB003147.

Plattner, G.-K., F. Joos, T. F. Stocker, and O. Marchal (2001), Feedback mechanisms and sensitivities of ocean carbon uptake under global warming, *Tellus Ser. B*, *53*, 564–592, doi:10.1034/j.16000889.

Plattner, G.-K., F. Joos, and T. F. Stocker (2002), Revision of the global carbon budget due to changing air-sea oxygen fluxes, *Global Biogeochem. Cycles*, *16*(4), 1096, doi:10.1029/2001GB001746.

Randerson, J. T., M. V. Thompson, T. J. Conway, I. Y. Fung, and C. B. Field (1997), The contribution of terrestrial sources and sinks to trends in the seasonal cycle of atmospheric carbon dioxide, *Global Biogeochem. Cycles*, *11*, 535–560.

Sarmiento, J. L., and N. Gruber (2006), *Ocean Biogeochemical Dynamics*, chap. 8, Carbon cycle, pp. 318–358, Princeton Univ. Press, Princeton, N. J.

Schmittner, A., A. Oschlies, H. D. Matthews, and E. D. Galbraith (2008), Future changes in climate, ocean circulation, ecosystems, and biogeochemical cycling simulated for a business-as-usual $CO_2$ emission scenario until year 4000 AD, *Global Biogeochem. Cycles*, *22*, GB1013, doi:10.1029/2007GB002953.

Schneider, B., M. Latif, and A. Schmittner (2007), Evaluation of different methods to assess model projections of the future evolution of the atlantic meridional overturning circulation, *J. Clim.*, *20*, 2121–2132, doi:10.1175/JCLI4128.1.

Schneider, B., L. Bopp, M. Gehlen, J. Segschneider, T. L. Frölicher, P. Cadule, P. Friedlingstein, S. C. Doney, M. J. Behrenfeld, and F. Joos (2008), Climate-induced interannual variability of marine primary and export production in three global coupled climate carbon cycle models, *Biogeosciences*, *5*(2), 597–614.

Steinacher, M., F. Joos, T. L. Frölicher, G.-K. Plattner, and S. C. Doney (2008), Iminent ocean acidification projected with the NCAR global coupled carbon cycle–climate model, *Biogeosciences Discuss.*, *5*(6), 4353–4393.

Stenchikov, G., K. Hamilton, R. J. Stouffer, A. Robock, V. Ramaswamy, B. Santer, and H.-F. Graf (2006), Artic oscillation response to volcanic eruptions in the IPCC AR4 climate models, *J. Geophys. Res.*, *111*, D07107, doi:10.1029/2005JD006286.

Stramma, L., G. C. Johnson, J. Sprintall, and V. Mohrholz (2008), Expanding oxygen-minimum zones in the tropical oceans, *Science*, *320*(5876), 655–658, doi:10.1126/science.1153847.

Volk, T., and M. I. Hoffert (1985), Ocean carbon pumps: Analysis of relative strengths and efficiencies in ocean driven atmospheric $CO_2$ changes, in *The Carbon Cycle and Atmospheric $CO_2$: Natural Variations Archean to Present, Geophys. Monogr. Ser.*, vol. 32, edited by E. T. Sundquist and W. S. Broecker, pp. 99–110, AGU, Washington, D. C.

Wang, Y. M., J. L. Lean, and N. R. Sheeley (2005), Modeling the sun's magnetic field and irradiance since 1713, *Astrophys. J.*, *625*, 522–538.

---

S. C. Doney, Marine Chemistry and Geochemistry, Woods Hole Oceanographic Institution, Woods Hole, MA 02543, USA.

T. L. Frölicher, F. Joos, and M. Steinacher, Climate and Environmental Physics, University of Bern, Sidlerstrasse 5, CH-3012 Bern, Switzerland. (froelicher@climate.unibe.ch)

G.-K. Plattner, Environmental Physics, Institute of Biogeochemistry and Pollutant Dynamics, ETH Zurich, Universittstrasse 16, CH-8092 Zurich, Switzerland.